*buildings*

MDPI

*Article*

# Experimental and Numerical Study Assessing the Synergistic Effect of Metakaolin and Waste Glass on the Concrete Mechanical and Structural Properties

**Ali Jahami [1], Hektor Frangieh [1], Joseph Assaad [1], Ahmad Alkhatib [2], Cigdem Avci-Karatas [3,*] and Nicola Chieffo [4]**

[1] Department of Civil and Environmental Engineering, University of Balamand, Tripoli P.O. Box 100, Lebanon; ali.jahami@balamand.edu.lb (A.J.); hector.frangieh.2002@gmail.com (H.F.); joseph.assaad@balamand.edu.lb (J.A.)
[2] Faculty of Civil Engineering, Aleppo University, Aleppo P.O. Box 4670, Syria; eng.alkhatib.ahmad@hotmail.com
[3] Department of Transportation Engineering, Faculty of Engineering, University of Yalova, 77200 Yalova, Türkiye
[4] Department of Engineering, School of Computing and Engineering, University of Huddersfield, Huddersfield HD1 3DH, UK; n.chieffo@hud.ac.uk
* Correspondence: cigdem.karatas@yalova.edu.tr; Tel.: +90-226-815-6486

## Abstract

This study presents a rigorous experimental and numerical investigation of the synergistic effect of metakaolin (MK) and waste glass (WG) on the structural performance of reinforced concrete (RC) beams without stirrups. A two-phase methodology was adopted: (i) optimization of MK and WG replacement levels through concrete-equivalent mortar mixtures and (ii) evaluation of the fresh and hardened properties of concrete, including compressive and tensile strengths, elastic modulus, sorptivity, and beam shear capacity. Five beam groups incorporating up to 30% MK, 15% WG, and 1% steel fiber were tested under four-point bending. The results demonstrated that MK enhanced compressive strength (up to 22%), WG improved workability but reduced ductility, and the combined system achieved a 13% increase in shear strength relative to the control. Steel fibers further restored ductility, increasing the ductility index from 1.338 for WG-only beams to 2.489. Finite Element Modeling (FEM) using ABAQUS with the Concrete Damage Plasticity (CDP) model reproduced experimental (EXP) load–deflection responses, peak loads, and crack evolution with high fidelity. This confirmed the predictive capability of the numerical framework. By integrating material-level optimization, structural-scale testing, and validated FEM simulations, this study provides robust evidence that MK–WG concrete, especially when fiber-reinforced, delivers mechanical, durability, and structural performance improvements. These findings establish a reliable pathway for incorporating sustainable cementitious blends into design-oriented applications, with direct implications for the advancement of performance-based structural codes.

**Keywords:** sustainable concrete; waste glass aggregate; metakaolin; reinforced concrete beams; finite element modeling (ABAQUS); steel fibers; earthquake-resistant design

check for updates

Academic Editor: Ali Hadigheh

Received: 8 August 2025
Revised: 29 August 2025
Accepted: 1 September 2025
Published: 4 September 2025

**Citation:** Jahami, A.; Frangieh, H.; Assaad, J.; Alkhatib, A.; Avci-Karatas, C.; Chieffo, N. Experimental and Numerical Study Assessing the Synergistic Effect of Metakaolin and Waste Glass on the Concrete Mechanical and Structural Properties. *Buildings* **2025**, *15*, 3185. https://doi.org/10.3390/buildings15173185

**Copyright:** © 2025 by the authors. Licensee MDPI, Basel, Switzerland. This article is an open access article distributed under the terms and conditions of the Creative Commons Attribution (CC BY) license (https://creativecommons.org/licenses/by/4.0/).

## 1. Introduction

Sustainability in civil engineering has become a crucial topic in modern construction, driven by the need to reduce environmental impact, optimize material usage, and enhance

the durability of structures [1–5]. The depletion of natural resources and accumulation of industrial waste necessitates the adoption of sustainable strategies that reduce the carbon footprint while maintaining the strength and performance of structures. This broad approach to sustainability encompasses various domains, including the development of low-carbon concrete [6,7], use of recycled materials in pavement engineering [8,9], and integration of green practices in structural design and urban infrastructure.

The use of waste-derived materials, such as industrial byproducts and recycled aggregates, has gained significant attention in sustainable construction practices [10–15]. Among these, waste glass (WG) offers dual environmental and technical benefits by reducing landfill dependency and cutting greenhouse gas emissions by up to 19% [15,16]. Previous studies have shown that the influence of WG on concrete depends strongly on the particle size, replacement level, and whether it substitutes supplementary cementitious materials or aggregates. Although the angular shape of WG particles may reduce workability, this drawback can be mitigated through optimized mix designs [17–19]. In the hardened state, the high silica content of WG ($\geq$70%) imparts pozzolanic activity, although concerns about alkali–silica reaction remain [15,17,18]. Finely ground WG (<100 μm) has been reported to refine the microstructure and enhance the density, durability, and strength [17,19], with improvements in compressive strength of up to 20% [15,18]. For instance, Nodehi et al. [16] observed a 7% increase in 91-day compressive strength with 20% WG, whereas Bhat et al. [17] demonstrated a ~22% increase in 28-day strength when 15% natural sand was replaced with crushed glass. Structural-level studies have also indicated benefits: Bawab et al. [18] found that WG enhanced the flexural performance of reinforced beams, and Zeybek et al. [19] showed a shear strength increase of 4.6% when fine aggregates were partially replaced by WG. However, performance declines were reported when coarse WG exceeded 10%, with up to 18% reductions in shear strength under wider stirrup spacings [19]. These mixed findings underscore the need for systematic investigations that not only optimize the WG content but also extend the analysis beyond material properties to structural performance, particularly under shear-dominated conditions.

Metakaolin (MK) is a highly reactive pozzolanic material produced by thermally activating kaolinite clay at 650–850 °C. Its fine particle size and amorphous silica enable secondary C–S–H formation, which enhances the strength and durability [20]. Numerous studies have shown that cement replacement with MK—typically up to 20%—can improve compressive strength through both pozzolanic and filler effects, with optimal gains often achieved between 10% and 15%, depending on the curing conditions [21–23]. However, higher replacement levels increase the water demand, necessitating the use of superplasticizers to maintain adequate workability [24]. In addition to strength, MK improves the resistance to sulfate attack, chloride ingress, alkali–silica reaction, and even high-temperature degradation up to 700 °C [25,26]. The densification effect has also been observed in combination with other SCMs, such as silica fume or fly ash, which further reduces porosity and refines the microstructure [17,20]. At the structural scale, Yerramala et al. [27] found that ferrocement incorporating 10% MK achieved early age flexural strength improvements of 44% in 7 days and ~35% at 28 days, while Arunakanthi et al. [23] reported consistent gains in compressive, tensile, and flexural strengths with substitutions of up to 15%. Overall, these findings demonstrate MK's dual role in advancing sustainable concrete technology by improving mechanical performance and durability while lowering $CO_2$ emissions [28,29]. Nevertheless, the majority of existing studies have concentrated on material-level properties, with limited investigations extending the evaluation of MK's benefits to RC structural members under shear or flexural loading, thereby leaving a gap in understanding its implications for the full-scale structural behavior.

Limited investigations have assessed the synergistic effects of MK and WG on the workability, strength, and structural performance of concrete mixtures. Nagrockiene and Paliulis [10] demonstrated that replacing 10% of cement with MK and 25% of sand with crushed WG could result in increased density, Ultrasonic Pulse Velocity (UPV), and resistance against frost attack [10]. These modifications contributed to increased compressive strengths, reaching 2.5% and 8.3% on 28 and 90 days, respectively. The presence of MK contributes to reduced water absorption and permeability, leading to a denser concrete matrix that is more resistant to aggressive environmental conditions [10]. Leal et al. [11] reported that the synergistic effect between MK and WG enables a more refined microstructure, as MK enhances pozzolanic reactions while the finely crushed WG contributes to reducing voids and porosity [11]. The authors suggested that the presence of MK in conjunction with WG can mitigate early strength reductions, as the pozzolanic activity of MK accelerates hydration and improves bonding within the cementitious matrix [11]. However, achieving an optimal balance remains crucial, as excessive MK (>20%) can lead to reduced workability and potential strength loss owing to increased dilution of the binder content. These insights highlight the need for precise mix-design considerations to maximize the benefits of WG and MK in concrete applications.

Unlike prior investigations that primarily examined the microstructural or durability aspects of metakaolin–waste glass (MK–WG) blends, this study advances the state of knowledge by focusing on the structural performance of RC beams without stirrups, in which shear behavior is the governing failure mode. While Nagrockiene and Paliulis [10] and Leal et al. [11] demonstrated improvements in density, compressive strength, and resistance to frost or permeability when MK and WG were combined, these studies did not extend their findings to structural elements subjected to shear stresses. The novelty of the present study lies in (i) establishing optimum MK and WG replacement levels using a concrete-equivalent mortar approach for practical mix design, (ii) experimentally (EXP) quantifying the coupled influence of MK and WG on both mechanical properties and shear strength of beams, (iii) proposing steel fiber incorporation as a targeted strengthening strategy to offset the ductility loss induced by WG, and (iv) validating the experimental results through Finite Element Modeling (FEM) simulations using ABAQUS. By linking material-scale modifications with full-scale structural behavior, this study provides new insights and design-oriented evidence on how MK–WG synergy can be effectively deployed in sustainable structural concrete, moving beyond the material-focused scope of earlier studies.

## 2. Experimental Program

### 2.1. Materials

ASTM C150 [30] Type I Portland cement (supplied by Cimenterie Nationale–Al SABEH Cement, Lebanon) and MK materials were used in this study. The cement had a Blaine fineness and characteristic 28-day compressive strength of 355 $m^2$/kg and 42.5 MPa, respectively. MK is artificially obtained by calcining kaolinitic clay and then ground to a fineness of 525 $m^2$/kg (i.e., considerably finer than cement). This aluminosilicate material is ideal for producing geopolymers, given its high SiO2 and Al2O3 contents of 56% and 38%, respectively. The specific gravities of the cement and MK are 3.15 and 2.22, respectively, and their loss on ignition is 1.95% and 1%, respectively. The naphthalene-based high-range water-reducing (HRWR) admixture had a specific gravity and solid content of 1.2 and 40%, respectively, and complied with ASTM C494 Type F [31]. Micro-filaments of steel fibers are employed; their length and diameter were 13 and 0.18 mm, respectively, leading to an aspect ratio of 72. The tensile strength of the fiber varied from 2400 to 2750 MPa.

Natural siliceous sand (i.e., fine aggregate) and crushed limestone coarse aggregates complied with the ASTM C33 specification [32]. The maximum particle size, water absorption, and bulk specific gravity of the sand were 4.75 mm, 0.95%, and 2.62, respectively. The maximum nominal coarse aggregate size, water absorption, and bulk specific gravity were 20 mm, 0.8%, and 2.72, respectively. A jaw crusher was used to break waste glass (WG) in the laboratory, which was then sieved mechanically over a 4.75-mm sieve opening to retain the fine passing fraction (i.e., similar to natural sand). The fineness moduli of the natural sand and WG are similar (2.36 and 2.15, respectively). The water absorption of WG is negligible, while its density is 2500 kg/m$^3$. Figure 1 presents the gradation curve of the WG used in this study.

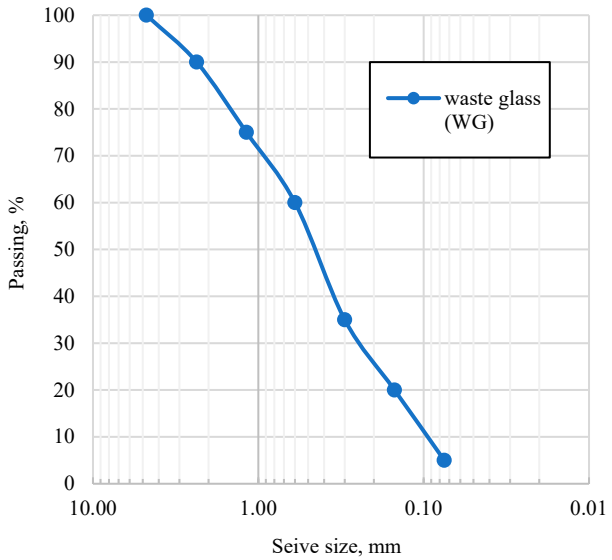



**Figure 1.** Gradation curve for the WG used.

### *2.2. Mortar and Concrete Proportions*

A normal-strength concrete grade commonly used in commercial and residential applications is considered in this work. Its cement content and water-to-binder ratio (w/b) are 375 kg/m$^3$ and 0.51, respectively, while its characteristic compressive strength is equal to 40 ± 2.5 MPa. The sand and coarse aggregate contents were 790 and 980 kg/m$^3$, respectively, which resulted in a sand-to-total-aggregate ratio of 0.45. The HRWR was adjusted to 1.4% of the cement mass to ensure a targeted workability of 200 ± 20 mm.

**Phase 1:** In order to simplify concrete batching and speed up the determination of the optimum MK and WG additions, testing in the first phase of this experimental program was performed using Concrete-Equivalent-Mortar (CEM) mixtures. The CEM method consists of similar concrete composition, with the coarse aggregates larger than 4.75 mm being replaced by an equivalent quantity of sand having a similar specific surface area [6,33]. The resulting cement, water, and sand contents were 375, 190, and 965 kg/m$^3$, respectively, with the HRWR fixed at 1.4% of the binder mass.

The cement was gradually replaced on a mass basis by MK at 5% increment rates, while the natural sand was replaced by WG at 2.5% increment rates until a specific set of workability and/or strength requirements are no longer satisfied. Hence, the variations in workability should not vary beyond ±10%, while the drop in strength should not exceed 12.5%. Such tolerances are consistent with the accepted practices in the concrete construction industry, as outlined in ACI 214-11: Guide to Evaluation of Strength Test Results of Concrete [34].

**Phase 2:** Five concrete mixtures are investigated in this program. Besides the control mix, two mixtures prepared using the optimized percentages of MK or WG are tested, while an additional mix containing both MK and WG is considered. As summarized in Table 1, the fine and coarse aggregates are adjusted in order to maintain a fixed sand-to-total-aggregate ratio of 0.45. The HRWR was also adjusted to secure the targeted workability. Finally, a fifth mix incorporating 1% steel fibers, by volume, is considered to compensate for the deficiency in tensile strength and ductility properties following the addition of MK and WG materials.

**Table 1.** Concrete mix proportions.

| Nomenclature | Control | 10% MK | 5% WG | 10% MK + 5% WG | 10% MK + 5% WG + 1% SF |
|---|---|---|---|---|---|
| Cement, kg/m$^3$ | 375 | 337.5 | 375 | 337.5 | 337.5 |
| MK, kg/m$^3$ | 0 | 37.5 | 0 | 37.5 | 37.5 |
| Water, kg/m$^3$ | 190 | 190 | 190 | 190 | 190 |
| Natural sand, kg/m$^3$ | 790 | 790 | 780 | 780 | 780 |
| WG (0–4.75 mm), kg/m$^3$ | 0 | 0 | 40 | 40 | 40 |
| Coarse aggregate, kg/m$^3$ | 980 | 980 | 980 | 980 | 980 |
| Steel fibers, kg/m$^3$ | 0 | 0 | 0 | 0 | 78.5 |
| HRWR, % of binder | 1.4 | 1.65 | 1.35 | 1.45 | 1.8 |

For mixing, the aggregate skeleton (i.e., sand, coarse aggregate, WG, and steel fibers) was homogenized together with half of mixing water. Cement (and MK) was then introduced with the remaining mixing water over a 2-min period, followed by the HRWR, which was adjusted to achieve the required slump. This mixing procedure proved effective in ensuring homogeneous dispersion of all inclusions (particularly WG and fibers) within the concrete matrix. After a resting period of 30 sec, the concrete is remixed for two additional minutes. Testing and sampling are carried out at room temperature of 22 $\pm$ 3 °C and relative humidity of 60 $\pm$ 10%.

### *2.3. Test Procedures*

The tests on fresh mortars included the workability determined after 15 drops on the flow table. The effect of MK or WG additions on mortar mechanical properties was assessed using 40 $\times$ 40 $\times$ 160-mm prisms, as per EN 196–1 [35], i.e., after the prisms are tested in flexure, the broken halves are tested in compression. Specimens are immersed in lime-saturated water until testing at an age of 28 days.

Tests on fresh concrete include slump and air content, while the hardened density, compressive strength (f'c), splitting tensile strength (ft), and secant modulus of elasticity (E) were determined using 100 $\times$ 200 mm cylinders as per ASTM C642 [36], C39 [37], C469 [38], and C496 [39], respectively. Averages of 3 to 4 values were considered for each property. The sorptivity of hardened concrete is determined in accordance with the ASTM C1585 [40]. The specimens measuring 100-mm diameter and 50-mm length are dried at 50 $\pm$ 3 °C to constant mass, and then immersed 2 $\pm$ 1 mm in water to determine the increase in mass over time resulting from water absorption. The sorptivity is calculated as the change in mass divided by the product of the specimen's cross-sectional area by water density.

The structural performance, including shear strength properties, is determined using RC beams measuring 150 mm $\times$ 150 mm in cross-section and 780 mm in length. The beams contained two 16 mm diameter longitudinal bars along with four stirrups positioned at the supports and loading points (Figure 2). The elastic modulus of steel (Es) was 200 GPa, while its yield stress (fy) and Poisson's ratio were 420 MPa and 0.3, respectively. The beams were mounted on a simply supported set-up and subjected to vertical loading applied at a

constant rate of 4 kN/min. Two LVDTs were positioned in the tension zone to determine the load-deflection curves. A high-definition portable microscope was used to detect the crack patterns in each beam.

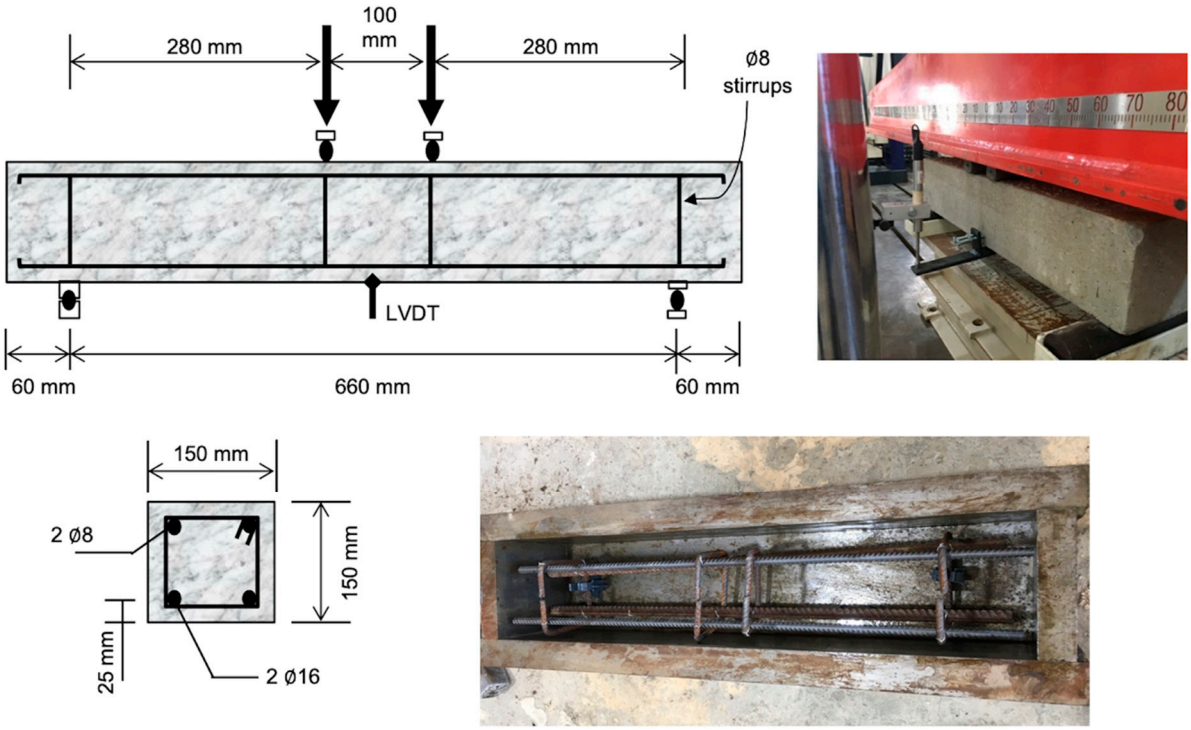



**Figure 2.** Set-up used for measuring the shear strength properties.

### *2.4. Finite Element Modeling*

The tested RC beam was modeled as a 3D deformable solid using C3D8R elements (i.e., 8-node linear brick elements with reduced integration and hourglass control), whereas the longitudinal reinforcement bars and stirrups were represented by T3D2 truss elements (i.e., 2-node linear elements designed to carry axial forces only). The rigid steel rods used for loading and support were modeled as R3D4 discrete rigid surfaces to accurately simulate the boundary conditions. A mesh sensitivity analysis was performed, and a 10 mm mesh size was chosen to ensure a balance between computational efficiency and result accuracy (Figure 3). The steel reinforcement was defined using a bilinear elastic–plastic material model, incorporating an initial elastic response up to the yield point, followed by a perfectly plastic plateau, which is a widely accepted approach for simulating RC behavior under monotonic loading. The steel properties, including the elastic modulus, yield strength, and strain-hardening characteristics, are detailed in Table 2 and Figure 4.

**Table 2.** Material properties of steel reinforcement used in the numerical model.

| Material Property | R8 | T16 |
|---|---|---|
| Density (kg/m$^3$) | 7850 | |
| Modulus of Elasticity (MPa) | 199,000 | 196,000 |
| Yield strength (MPa) | 580 | 575 |
| Yield strain (%) | 0.290 | 0.290 |
| Ultimate strength (MPa) | 660 | 750 |
| Ultimate strain (%) | 13.5 | 14 |

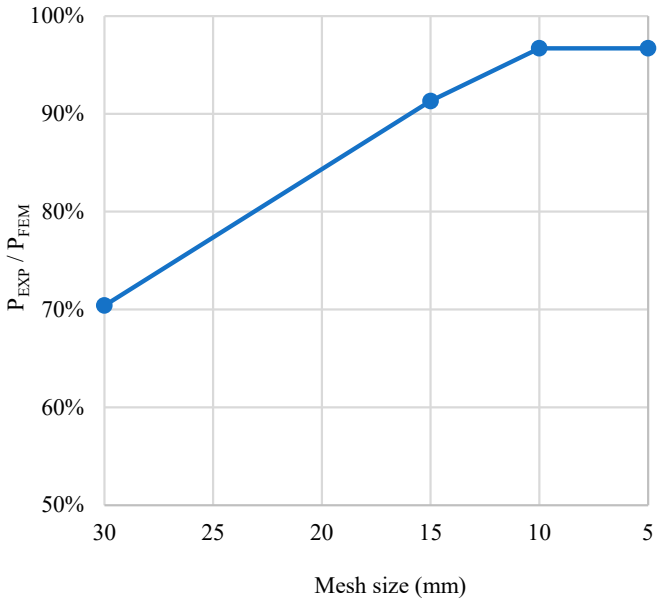



**Figure 3.** Mesh sensitivity analysis results ($P_{EXP}/P_{FEM}$ vs. mesh size).

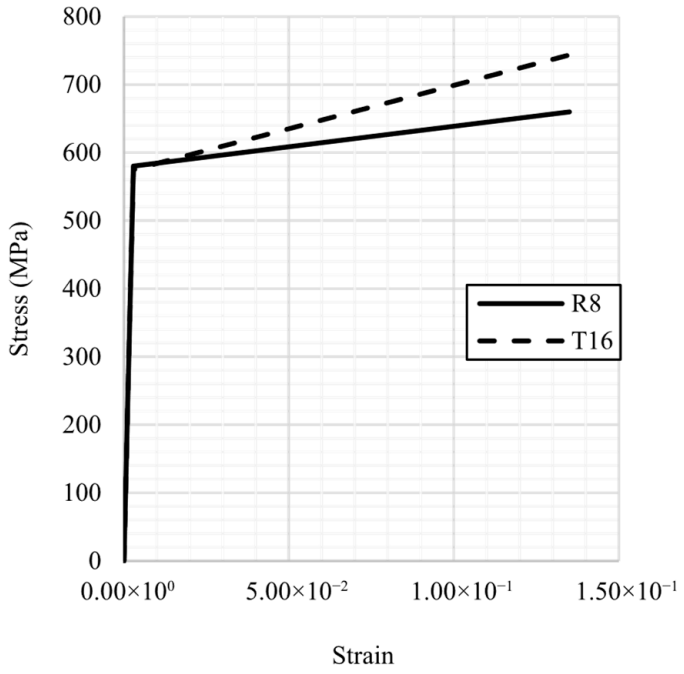



**Figure 4.** Stress-strain curves for steel rebars as defined in ABAQUS.

The concrete material was simulated using the Concrete Damage Plasticity (CDP) material model available in ABAQUS, which effectively captures both compressive crushing and tensile cracking under monotonic and cyclic loading conditions. This model requires the definition of key material parameters, such as the dilation angle, flow potential eccentricity, stress ratios, and viscosity parameter. In addition, the tensile and compressive responses of concrete are specified through the stress–strain curves. The specific values adopted for these parameters are listed in Table 3. The CDP model is well established for representing concrete failure mechanisms and has been extensively validated in literature [41]. Figure 5 shows the CDP-based stress–strain curves for all the concrete mixes.

**Table 3.** Concrete Damage Plasticity (CDP) model parameters.

| Material Property | |
|---|---|
| Dilation angle (deg) | 35–42 |
| Eccentricity | 0.1 |
| $f_{bo}/f_{co}$ | 1.16 |
| K | 0.667 |
| Viscosity parameter | 0.0001 |

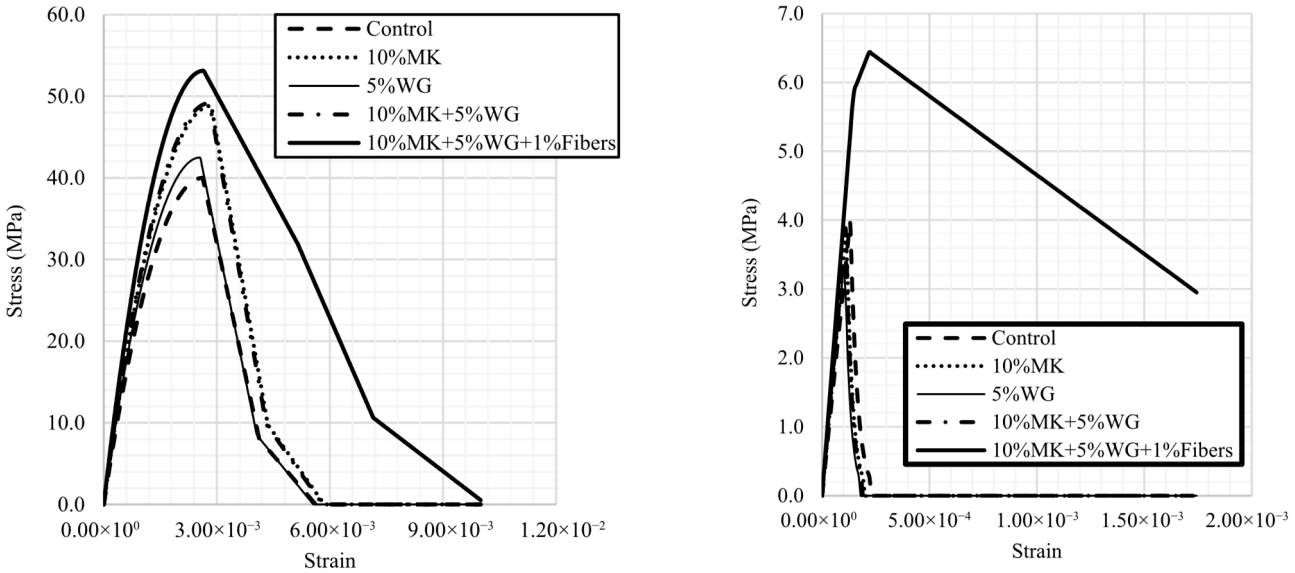



**Figure 5.** Stress-strain curves for concrete mixes as defined in ABAQUS. (**a**) Concrete behavior in compression. (**b**) Concrete behavior in tension.

To model concrete damage in CDP, the tensile and compressive damage variables were derived directly from the adopted σ–ε laws and the initial elastic modulus ($E_0$). For each point on the curves, the inelastic strain measure required by ABAQUS was computed as $\epsilon^{in} = \epsilon - \frac{\sigma}{E_0}$ (cracking strain in tension; inelastic strain in compression), and the associated damage was obtained from the stiffness degradation relation $\sigma = (1-d)E_0(\epsilon - \epsilon^{in})$, i.e., $d = 1 - \frac{\sigma}{E_0(\epsilon - \epsilon^{in})}$. In tension, a tension-stiffening law was used: linear elastic up to $\varepsilon_{t0} = f_t/E_0$, followed by softening regularized with the crack-band approach so that the area under the $\sigma - w$ curve equals the tensile fracture energy $Gf$ (with $w \approx \ell_{ch}\varepsilon^{ck}$ and $\ell_{ch}$ taken as the characteristic element length). This yields a $d_t(\varepsilon^{ck})$ value consistent with the chosen softening shape (exponential for plain mixes and bilinear with higher residual for the steel-fiber mix). In compression, the hardening/softening branch was defined from the Hognestad-type curve, converted to $\varepsilon^{in}$, and computed $d_c(\varepsilon^{in})$ by the same degradation relation; the post-peak slope was chosen to match the observed ductility (a gentler post-peak slope for the fiber-reinforced mix.). Further details can be found in Figure 5.

The support conditions were modeled using rigid plates, with pin supports applied at the beam ends to restrain all translational degrees of freedom (X, Y, and Z). The loading rollers at the top of the beam were constrained in all directions except the Y-direction, allowing for controlled vertical displacement during loading. Figure 6 presents the boundary conditions and geometry of the 150 × 300 × 1600 mm beam used as a representative model. Loading was applied through two rollers to simulate a four-point bending test, using a displacement-controlled protocol in which displacement increased gradually from zero to a maximum value corresponding to experimental failure limits. The loading step

was executed using the *Dynamic Explicit* solver in ABAQUS, which is well-suited for handling material nonlinearity, extensive cracking, and convergence difficulties commonly encountered with static solvers [42].

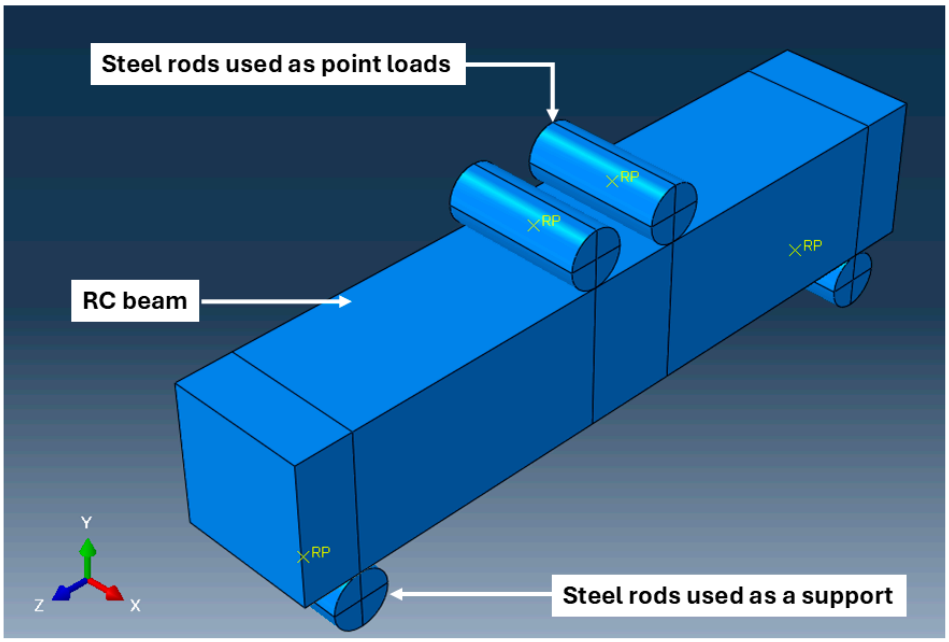



**Figure 6.** 3D finite element model of the RC beam (RP: Reference point in ABAQUS).

In the numerical model, two types of interactions were defined to accurately simulate the behavior of RC beams. The interaction between concrete and reinforcing steel was modeled using the *Embedded Region* constraint in ABAQUS, ensuring a perfect bond with no relative slip, consistent with experimental observations that showed no signs of bond failure throughout the loading process. For the interaction between the concrete body and rigid surfaces representing supports and loading plates, a general contact formulation was adopted. A "hard" contact was defined in the normal direction to prevent interpenetration, while a penalty-based friction model with a calibrated coefficient of 0.2 was used in the tangential direction to simulate shear resistance. This configuration enabled realistic representation of support constraints and load transfer conditions, closely aligning with experimental results.

## 3. Results and Discussion

### *3.1. Phase 1: Mortar Fresh and Hardened Properties*

Figure 7 illustrates the effect of partially replacing the fine aggregate by WG and cement by MK on the flow of freshly mixed mortars. The dashed lines at ±10% denote the industry-accepted workability tolerance [33] in order to ensure the proper handling, placement, and finishing at the jobsite. As shown, the flow tends to gradually increase with 2.5% to 10% WG additions, while remaining within the 10% allowable range. This can be attributed to the WG smooth surface and low water absorption, promoting internal lubrication and improved flow. Similar behavior was observed in Self-Compacting Concrete (SCC) mixes, where the slump flow improved as the glass content increased [43]. However, when the WG replacement reached 15%, the flow increased considerably above the threshold limitation. While this may seem attractive during concrete pouring of congested and difficult access members, the increased workability often necessitates adjustment of the mix design to maintain good homogeneity and reduce the risks of bleeding and segregation [6,33].

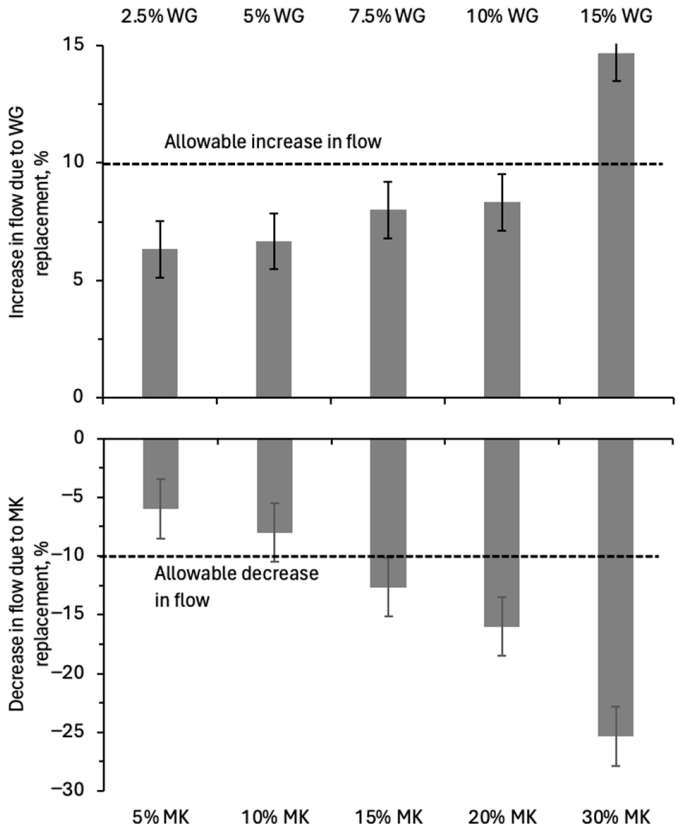



**Figure 7.** Variation in mortar flow with increased replacement ratios of fine aggregate by WG and cement by MK.

In contrast to WG additions, the incorporation of MK led to reduced flow, which can mainly be ascribed to fine particles that increase the binder compacity and water demand. Hence, the flow slightly decreased with 5–10% MK, while remaining within the −10% threshold limit. At 15–30% MK, the flow declines sharply below the −10% threshold. This finding is consistent with earlier studies [44], wherein the high MK content impairs workability because of its fine particles and high-water demand. Although the allowable MK replacement rate can be set at 10%, it is interesting to note that the combination of WG and MK in the same mixture can reduce the variations in workability, especially given their opposing effects on flow.

Figure 8a,b show the percentage change in 28-day compressive strength (f′c) and flexural strength (fr) resulting from the incremental replacement of (a) cement by MK and (b) fine aggregate by WG. The horizontal dashed line indicates the −12.5% allowable limit in concrete practice, beyond which the drop in strength becomes unacceptable [33]. For mortars with 2.5% and 5% WG, both f′c and fr remained within the acceptable range of strength reductions. This trend is attributed to the improved particle packing density and pozzolanic properties of the finely ground WG, which can contribute to matrix densification and minor strength changes [45]. With increased WG replacement of 7.5% and 10%, the strength decreased sharply beyond the permissible threshold of −12.5%. This is likely due to the non-reactive nature and smooth surface of the WG particles, which leads to poor bond development in the interfacial transition zone (ITZ). In other words, this suggests that the WG replacement should be limited to 5%.

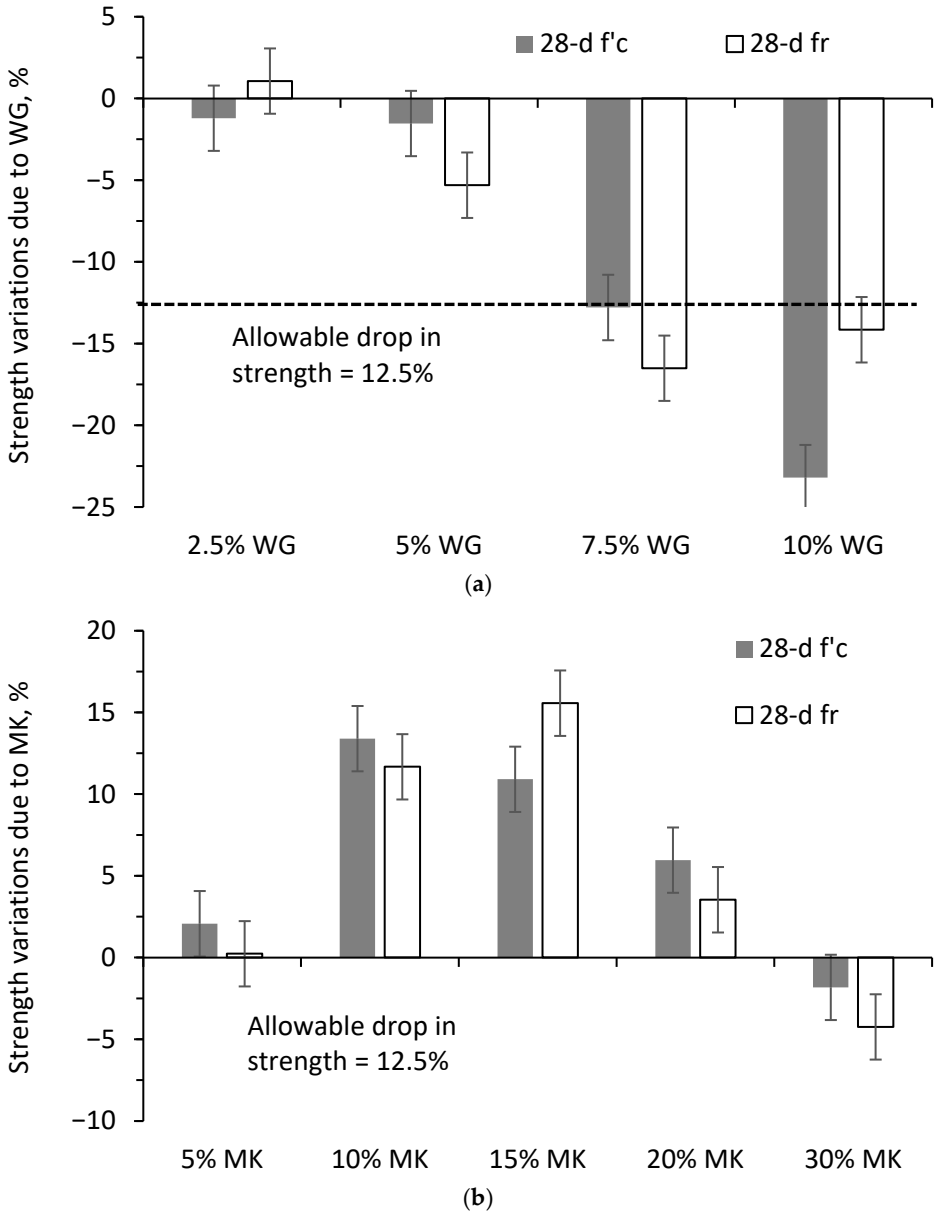



**Figure 8.** Percentage change in the 28-day f′c and fr for mixtures incorporating (**a**) WG as fine aggregate and (**b**) MK as cement replacement.

The f′c and fr responses followed an increasing trend for mortar mixtures prepared with 5–15% MK, which then gradually decreased at higher MK replacement rates. The strength enhancement agrees with the literature, wherein fine MK particles combined with their pozzolanic activity can refine the pore system and create additional CSH hydrates, leading to improved mechanical properties [46,47]. The strength begins to decline as the replacement ratio reaches 20–30%, although it is still within tolerances, which can be attributed to the dilution effect and potential microcracking due to shrinkage cracks [48]. Based on the flow and strength responses (Figures 7 and 8), it can be concluded that the optimum cement replacement by MK and fine aggregate by WG is 10% and 5%, respectively.

### *3.2. Phase 2: Concrete Mechanical Properties*

The HRWR demand to reach the targeted slump, as well as the concrete hardened density, $f'_c$, $f_t$, $E$, and sorptivity responses, is summarized in Table 4. The table also presents the RC shear strength properties including the ultimate load at failure ($P_{max}$), deflection

at failure ($\delta_{max}$), and ductility index (μ). The latter is determined as the ratio between the displacement at 90% $P_{max}$ on the post-peak region of the load vs. deflection curves with respect to the displacement at the same load (i.e., 90% $P_{max}$) on the pre-peak region (Figure 9); higher values reflect greater ductility at failure [49].

**Table 4.** Concrete hardened plain and shear strength properties.

| Property | Control | 10% MK | 5% WG | 10% MK + 5% WG | 10% MK + 5% WG + 1% Fibers |
|---|---|---|---|---|---|
| HRWR, % of binder | 1.4 | 1.65 | 1.35 | 1.45 | 1.8 |
| Density, kg/m$^3$ | 2439.5 | 2415.9 | 2401.1 | 2429.3 | 2476.6 |
| 7-d f'c, MPa | 29.78 | 29.26 | 30.61 | 37.49 | 45.54 |
| 28-d f'c, MPa | 40.00 | 48.84 | 42.51 | 49.18 | 53.14 |
| ft, MPa | 4.00 | 3.88 | 3.48 | 3.87 | 5.86 |
| E, GPa | 30.47 | 34.25 | 33.21 | 35.02 | 40.11 |
| Sorptivity, mm/hr$^{0.5}$ | 0.393 | 0.255 | 0.36 | 0.167 | 0.214 |
| $P_{max}$, kN | 69.77 | 74.33 | 72.18 | 79.08 | 88.96 |
| $\delta_{max}$, mm | 3.45 | 4.62 | 1.32 | 2.66 | 3.77 |
| Ductility index | 1.513 | 1.807 | 1.338 | 1.695 | 2.489 |

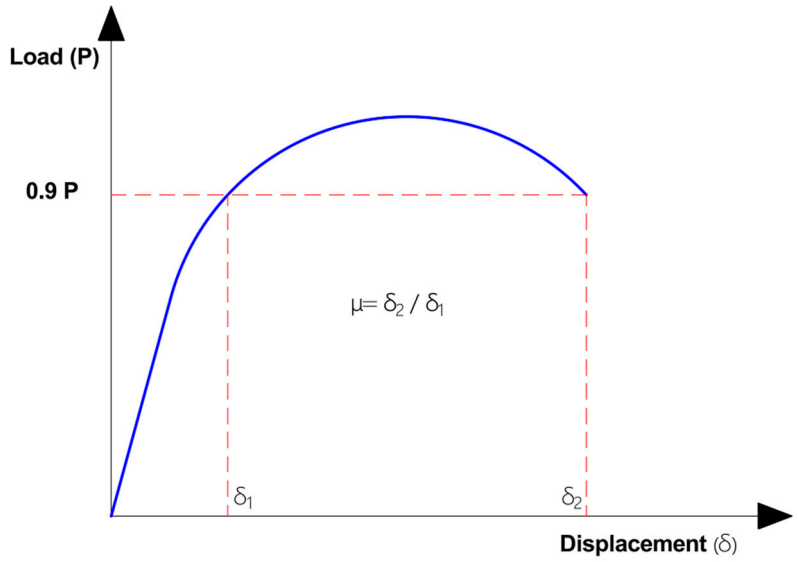



**Figure 9.** The ductility index (μ) concept.

### 3.2.1. Plain Concrete Properties

The HRWR demand increased from 1.4% to 1.65% with the addition of MK. This can be attributed to the considerably higher MK fineness (vs. cement), which requires additional superplasticizing molecules to deflocculate the matrix and ensure the targeted slump. In contrast, the HRWR dropped to 1.35% when WG was used, given their smoother surfaces (vs. natural sand) that enhanced the ease of flow [50]. As expected, the incorporation of steel fibers appeared to worsen the concrete workability through increased internal friction within the aggregate skeleton [51], which necessitated the highest HRWR demand of 1.8%. Generally, the density of hardened concrete did not vary significantly with MK and/or WG additions compared to the control value of 2439.5 kg/m$^3$.

Figure 10 shows the 28-day $f'_c$ and $f_t$ responses for the tested concrete mixtures. As shown, $f'_c$ increased in all modified mixes compared to the control mix (40 MPa), with the highest value recorded for the mix containing MK, WG, and steel fibers. The concrete prepared with 10% MK showed a significant strength gain (48.8 MPa) compared to the control value. This can be attributed to the MK fineness that enhances the density

and compacity of the binder phase, coupled with some pozzolanic reactions that create additional CSH hydration compounds that strengthen the cement matrix [52]. The $f'_c$ of concrete prepared with 5% WG (42.5 MPa) remained within the repeatability of the testing, given the relatively coarse particle sizes. Harrison et al. [53] reported that the addition of 5%, 10%, and 15% glass particles to SCC mixtures reduced the flexural strengths by 2%, 3.7%, and 6.8%, respectively, and f'c by averages of 6.1%, 15.2%, and 20%, respectively. Some studies have reported that finely ground WG can be used as a microfiller to enhance the packing density, while its glassy inert nature limits pozzolanic reactions [54]. Concrete containing both MK and WG showed a remarkable increase in $f'_c$ to 49.2 MPa, reflecting their positive benefits on strength development. The highest $f'_c$ reached 53.1 MPa when steel fibers were added to the WG and MK materials, which can be ascribed to the increased bridging and confinement effects that reduce microcrack initiation and propagation [55].

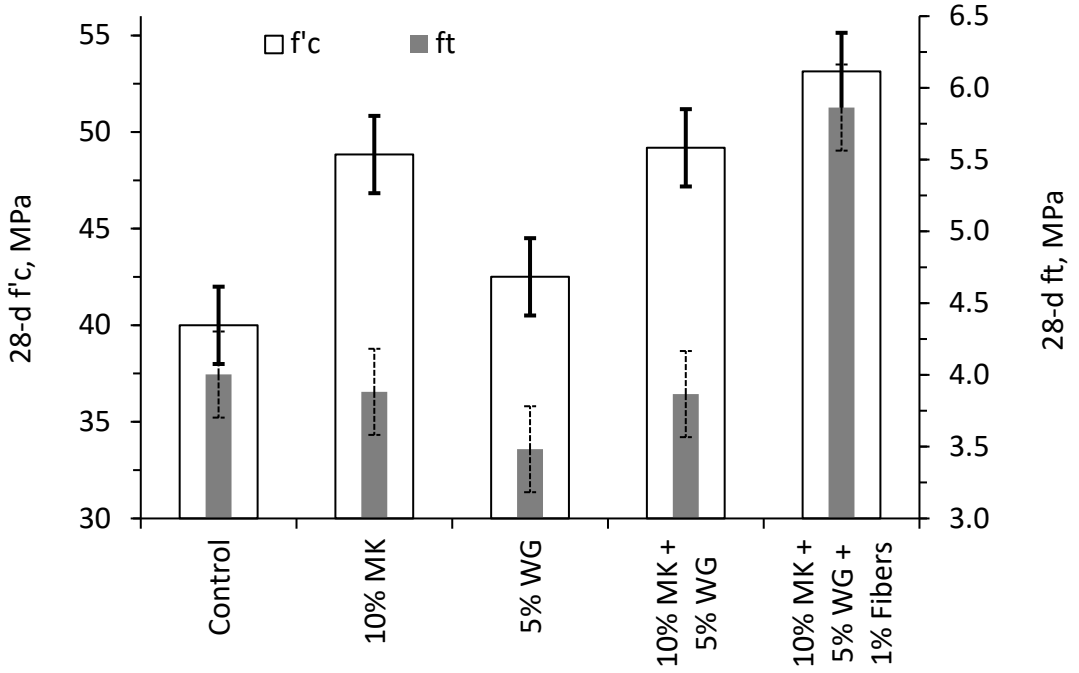



**Figure 10.** Compressive and splitting tensile strength for concrete mixes.

As shown in Figure 10, the ft for the control mix was 4.00 MPa at 28 days, while the concrete containing WG exhibited the least ft of 3.48 MPa. As discussed earlier, this can be related to the relatively coarse glass particle sizes, including the poor bonding at the aggregate-paste interfaces owing to their smooth surfaces, which can promote the formation of cracks and slippage during loading [17]. The ft was partially recovered to 3.87 MPa when both MK and WG were incorporated, while this significantly increased to 5.86 MPa with steel fiber additions. The presence of fibers is particularly efficient in bridging cracks and absorbing the stresses created during tensile loading [56]. Notably, the deteriorated $f'_c$ and $f_t$ responses owing to the WG addition were considerably restored when the WG was combined with MK in the same concrete, reflecting the synergistic effect of both materials.

Compared to the control $E$ value of 30.5 GPa, the incorporation of MK and/or WG led to relatively increased responses, reaching 34 $\pm$ 1 GPa. These results are aligned with the modest improvement in $f'_c$ responses, indicating that such additions are efficient in densifying the cement matrix, either due to the filler or pozzolanic effects. The highest $E$ improvement (40.1 GPa) resulted from the concrete containing MK, WG, and steel fibers,

reflecting the benefits of combining these three materials to improve stiffness and load resistance owing to the refined cement microstructure and stronger concrete skeleton [37].

Figure 11 shows the water absorption measurements as a function of the square root of time for the control, 10% MK, and 10%MK + 5%WG mixtures. The resulting initial rate of water absorption (given in mm/hr$^{0.5}$) is determined as the slope of the straight line fitted to the data points determined during the first six hours of measurements. Clearly, the sorptivity remarkably dropped from 0.393 mm/hr$^{0.5}$ for the control mix to 0.255 and 0.167 mm/hr$^{0.5}$ when the MK or the combination of MK and WG are respectively used, indicating superior performance mostly ascribed to the filler and pozzolanic effects of the MK additions. The sorptivity of the mix containing 5% WG was close to the control value (i.e., 0.36 mm/hr$^{0.5}$). Although the intrinsic water absorption of WG is almost nil, earlier studies have shown that the poor bonding between such waste plastic or glass additions and the cement matrix can facilitate water ingress by capillarity in hardened concrete [57,58].

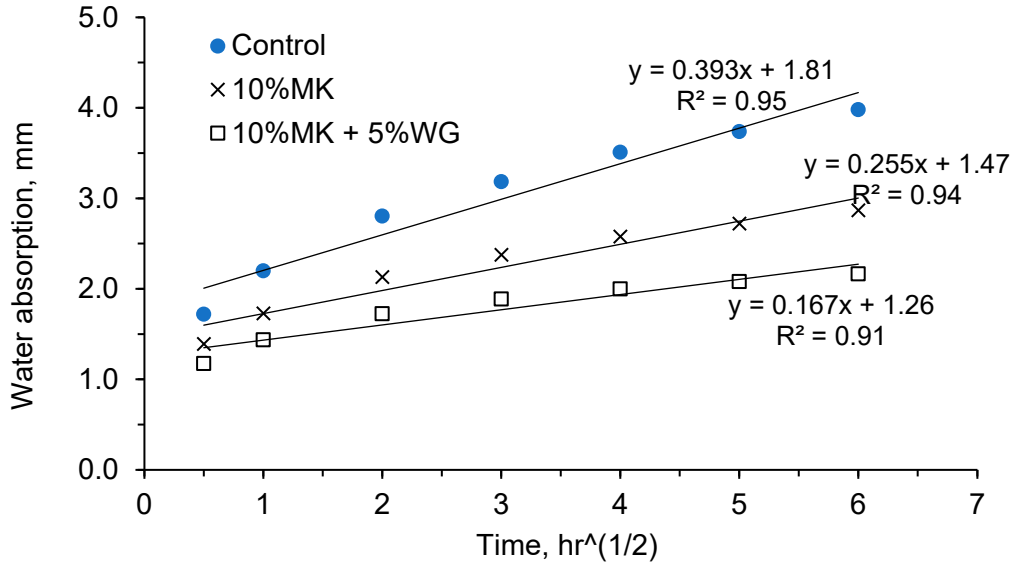



**Figure 11.** Sorptivity test results for concrete mixes.

### 3.2.2. Shear Strength Properties

The crack patterns observed after failure of the RC beams containing MK and/or WG additions are shown in Figure 12. Generally speaking, the failure of all beams occurred after the formation of a major diagonal shear crack, which gradually propagated at an angle of about 45 degrees from the horizontal towards the compression zone. Unlike the other specimens, the mix containing 5% WG displayed only one shear crack with very few fine cracks on the beam surface. This pattern corresponds to the brittle behavior observed in the load–displacement curve (discussed later), indicating that the smooth surface and poor bonding of WG with the cement matrix promote crack formation and slippage during loading.

The load versus displacement curves recorded for the various tested RC beams are plotted in Figure 13. As shown, the load gradually increased in the elastic region, which can be associated with dowel action resulting from the longitudinal steel bars along with an aggregate interlock mechanism responsible for shear transfer in RC beams without stirrups [59]. The latter phenomenon occurs along the diagonally fractured surface and is believed to mitigate sudden failure by transferring up to 50% of the applied shear force to the surrounding concrete.

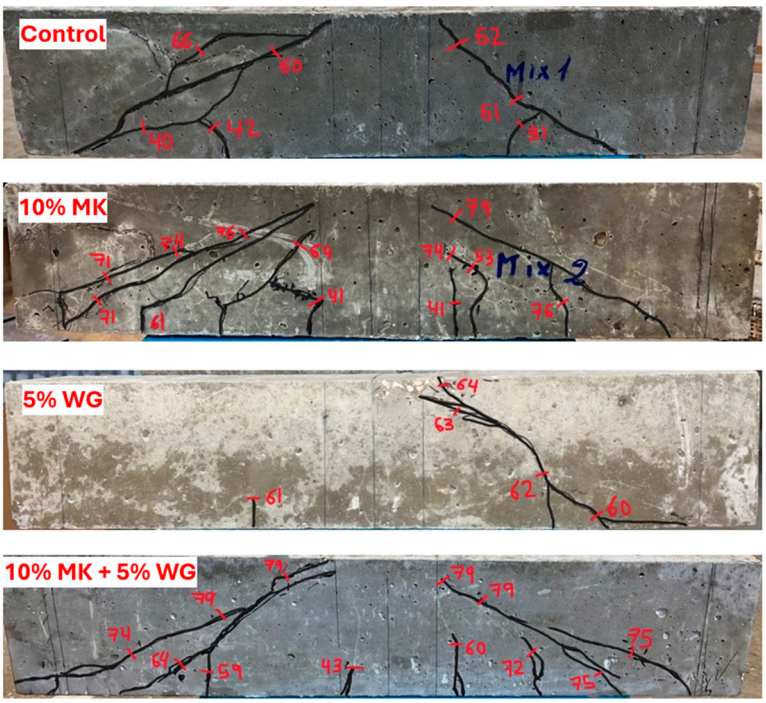



**Figure 12.** Failure patterns and shear crack distribution for beams. (The handwritten numbers indicate the sequence of major cracks formed during testing, while Mix1 and Mix2 denote the specimen identification.).

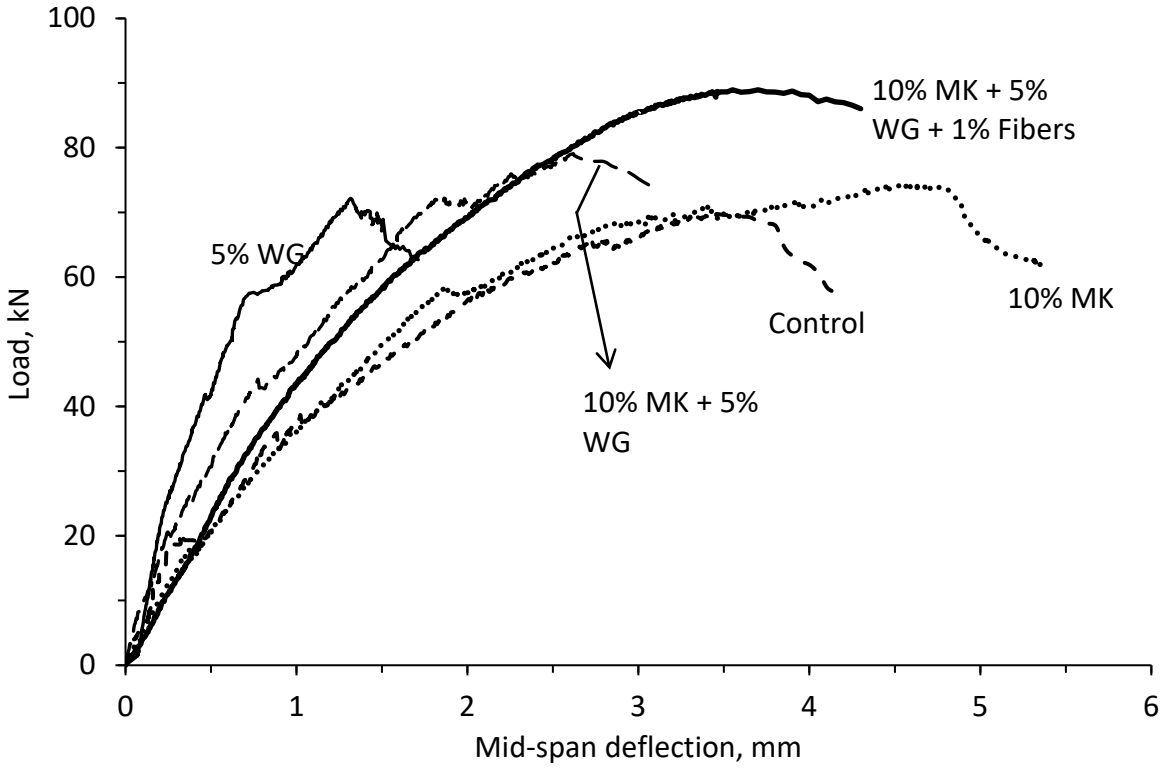



**Figure 13.** Experimental load vs. deflection curves for beams without shear reinforcement.

The elastic region continued until the beam stiffness began to deteriorate, which increased the rate of mid-span deflection accompanied by widening of the diagonal cracks in size and propagation deep in the compression zone until reaching the ultimate load capacity ($P_{max}$). The lowest $P_{max}$ of 69.8 kN was recorded for the control beam, whereas it

increased with MK and/or WG additions (Table 4). Hence, a $P_{max}$ of 72.2 kN was obtained with the use of 5% WG, whereas it reached 74.3 and 79.1 kN for the beams containing 10% MK and the combination of both MK and WG, respectively. The corresponding increases in $P_{max}$ were 3.5%, 6.5%, and 13.3%, respectively. These results are consistent with the concrete mechanical properties, particularly the beneficial synergistic effect between MK and WG. The highest $P_{max}$ of 88.9 kN was achieved when 1% steel fibers were incorporated, leading to an increase of 27.5%. This improvement can be primarily attributed to the fiber-bridging effect, which restricts crack widening and enhances the aggregate interlock mechanism during the loading process [60]. Al Ghali et al. [61] reported that the presence of fibers transmits the stresses to surrounding concrete, thus fostering higher energy transfer prior to beam destruction.

The mid-span deflection at failure ($\delta_{max}$) was 3.45 mm for the control beam and considerably dropped to 1.32 mm for the beam containing 5% WG. The ductility index (μ), calculated as the ratio of the displacements at 90% Pmax in the post- and pre-peak regions, varied from 1.513 to 1.338, respectively. As previously explained, this reduction can be attributed to the smooth surface of the WG particles, which weakens the bond with the cement paste and promotes slippage, leading to a more abrupt decrease in the post-peak response. Structurally perspective, a lower ductility index indicates a reduced capacity of the material to undergo large deformations before failure, which could limit the ability of real structures to dissipate energy under extreme loading conditions, such as earthquakes or impact loads.

As shown in Figure 13, $\delta_{max}$ increased to 3.77 mm with the incorporation of steel fibers, and the resulting μ increased to 2.489. These results confirm the beneficial role of fibers in bridging cracks and enhancing energy absorption, thereby restoring ductility and improving the structural resilience of concrete elements containing WG [62]. It is to be noted that $\delta_{max}$ dropped to 2.66 mm for the concrete beam prepared with both MK and WG, while the corresponding μ equaled 1.695. This intermediate ductility reflects a partial improvement owing to MK but still underscores the importance of designing mixes that balance strength, ductility, and long-term performance when applied to real structures.

#### 3.2.3. Finite Element Results

Finite element modeling (FEM) offers a powerful framework for predicting the performance of RC beams and other structural members. Figure 14 plots typical load-deflection curves determined numerically via ABAQUS using the Concrete Damage Plasticity (CDP) model, while Table 5 summarizes the predicted $P_{max}$, $\delta_{max}$, ductility index, and percentage of damaged zone. This index reflects the concrete zones where the tensile stresses exceed the actual concrete tensile strength at failure.

**Table 5.** Shear strength properties determined numerically using ABAQUS.

| Output | Control | 10% MK | 5% WG | 10% MK + 5% WG | 10% MK + 5% WG + 1% Fibers |
|---|---|---|---|---|---|
| $P_{max}$, kN | 66.1 | 71.6 | 76.8 | 78.8 | 89.8 |
| $\delta_{max}$, mm | 5.19 | 6.13 | 1.47 | 3 | 4.5 |
| Ductility index | 2.21 | 2.73 | 1.41 | NA | NA |
| Damaged zone, % | 42.6 | 46.7 | 41.8 | 47 | 51.4 |

Generally, the load–deflection curves determined using ABAQUS closely matched those obtained experimentally (EXP). For example, the predicted peak load of the control beam was 66.1 kN, which is close to the experimental value of 69.77 kN. The slight overprediction in displacement (5.19 mm vs. 3.45 mm) can be attributed to FEM assumptions of

idealized material behavior, where crack localization and aggregate bridging are not fully captured, leading to smoother post-peak softening.

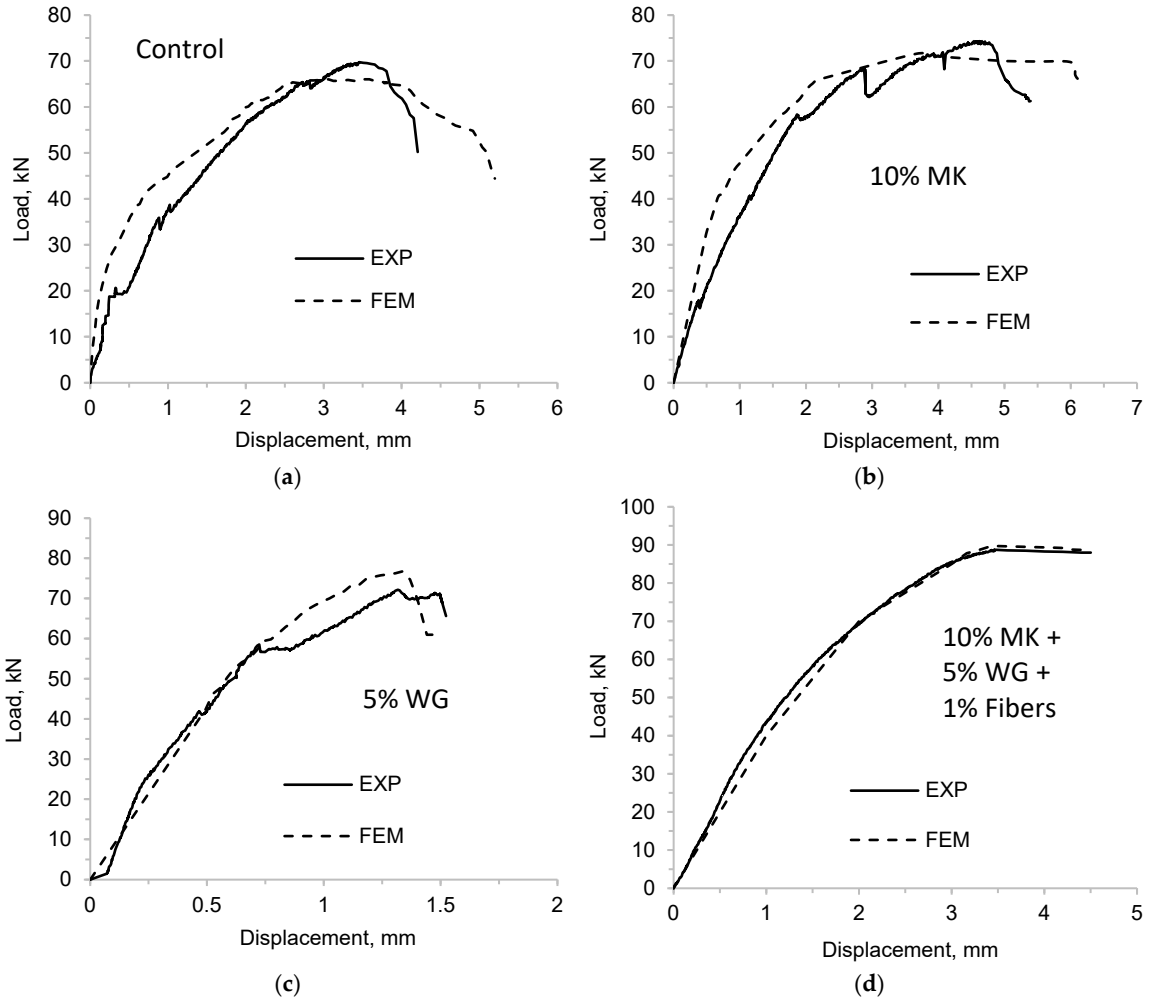



**Figure 14.** Comparison of load vs. displacement curves determined experimentally vs. numerically.

The agreement between the FEM and experimental results persisted with the inclusion of 10% MK. Numerically, the beam reached a peak load of 71.6 kN, showing excellent alignment with the experimental value of 74.33 kN. The enhanced matching can be ascribed to the pozzolanic activity of MK, which reduces the cement matrix variability and makes the actual behavior more predictable. The ductility index increased from 1.807 (EXP results) to 2.73 (FEM results), indicating that the FEM slightly overpredicted the post-peak deformation capacity compared to the experimental observations. Similarly, the beams containing 5% WG exhibited excellent matching, as the FEM model predicted a peak load (76.8 kN) and displacement (1.47 mm) close to the experimental values (72.18 kN and 1.32 mm). The ductility index slightly varied from 1.41 by FEM to 1.338 by EXP. Thus, it can be concluded that the CDP model is capable of simulating the progressive and abrupt damage resulting from the incorporation of MK or WG. This complements the CDP model assumptions to idealize stress redistribution and better simulate the crack development, including the pre- and post-peak behaviors, with enhanced accuracy.

The hybrid beam made of 10% MK and 5% WG demonstrated a notable matching in FEM–EXP correlation, owing to the compensatory interaction between the two additions. The numerical peak load of 78.8 kN and displacement of 3.0 mm closely aligned with the experimental values (79.08 kN and 2.66 mm). The numerical ductility index was

not reported in this case because of the improved post-peak behavior of the load versus displacement curve. This underscores the FEM strength in modeling well-compensated, homogenous systems, where the assumptions of isotropy and damage softening hold more accurately. On the other hand, a remarkable agreement is achieved in the beam incorporating 10% MK, 5% WG, and 1% steel fibers; the FEM peak load of 89.8 kN and displacement of 4.5 mm are close to the experimental results of 88.96 kN and 3.77 mm. This high level of consistency is attributed to the mechanical contribution of steel fibers, which bridge microcracks and improve stress redistribution. This behavior enhanced structural ductility, leading to smoother and more stable post-peak responses calibrated using the CDP model.

Figure 15 shows the damage zones determined at $P_{max}$ for the control beam and those containing MK, WG, or a combination of these with 1% steel fibers. The scale varies from 0 to 1, whereby a value of 0 refers to undamaged concrete (i.e., blue areas), while increased values progressively indicate the crack positioning and damage level (i.e., green, yellow, and then red). The spatial pattern of the FEM damage contours mirrored the tests, that is, a dominant diagonal shear band extending from the support toward the point load, accompanied by secondary flexural cracks in the tension zone. This agreement confirms that the CDP model reproduced the observed failure mechanism across all mixes.

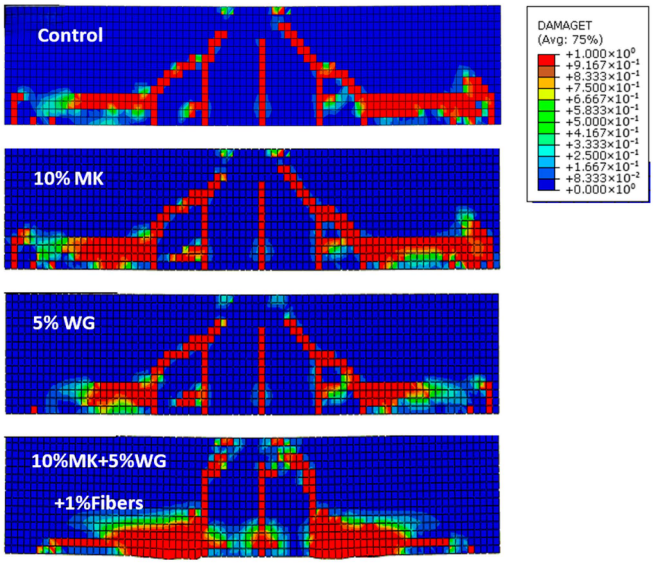



**Figure 15.** Damaged zones determined by numerical modeling at $P_{max}$.

The analysis of the damage zone coverage based on FEM visualizations revealed that the control beam exhibited the smallest damaged area, covering approximately 42.6% of the total surface, which indicated a more localized failure pattern. The incorporation of 10% MK increased the damaged zone to approximately 46.7%, reflecting enhanced stress distribution and wider crack propagation. In contrast, the introduction of 5% WG reduced the damage zone to 41.8%, which can be attributed to the smooth nature of such additions that increase slippage and lead to an abrupt drop without the creation of wider cracks. The most extensively damaged area appeared in the hybrid mix containing MK, WG, and 1% steel fibers, reaching 51.4%. This wider damage distribution is consistent with the known crack-bridging and energy dissipation capabilities of the fibers, which promote gradual failure and activate more of the cross-section [63]. Overall, the increase in the damaged area correlated with the improved ductility and redistribution of load observed in the numerical simulations. These observations align with previous studies that emphasized the role of experimentally calibrated numerical models in predicting the nonlinear

response of structural members [63,64]. In particular, Avci-Karatas et al. [64] demonstrated that FEM-based simulations, when validated against full-scale experimental data, can robustly capture post-peak behavior and damage progression in earthquake-resistant structural systems.

## 4. Conclusions

This study experimentally and numerically investigated the synergistic effect of metakaolin (MK) and waste glass (WG) on the performance of reinforced concrete (RC) beams without stirrups. This study combined mortar-level optimization, beam-scale testing, and ABAQUS numerical simulations to link material-level modifications with full structural behavior. These findings provide valuable insights into how sustainable cementitious blends can influence the strength, ductility, and service performance of structural elements.

The following conclusions can be drawn:

1. Mortar testing demonstrated that the optimum replacement levels are 10% MK and 5% WG, balancing improved strength and workability while avoiding excessive dilution or bond loss. This validates the Concrete-Equivalent Mortar (CEM) approach as a practical screening tool for sustainable mix design.
2. At the concrete scale, MK enhanced compressive strength and reduced sorptivity, while WG improved workability but decreased ductility when used alone. The combined MK–WG system achieved a 13% increase in shear strength relative to the control mix, demonstrating clear benefits in structural performance.
3. Beams with 5% WG alone exhibited a reduced ductility index ($\mu = 1.338$), reflecting a brittle response that could limit energy dissipation in real structures. The incorporation of steel fibers effectively mitigated this issue, raising $\mu$ to 2.489 and restoring resilience, a critical feature for seismic or impact-resistant design.
4. The ABAQUS Concrete Damage Plasticity (CDP) model closely reproduced the experimental results, confirming its reliability in simulating load–deflection behavior, crack evolution, and ductility variations. This provides a predictive framework for extending laboratory findings to large-scale applications.

The findings of this study emphasize that MK–WG concrete, especially when combined with steel fibers, can enhance shear strength, refine durability, and restore ductility, thereby offering a credible pathway for integrating sustainable materials into structural design practice. Such outcomes have direct implications for performance-based design codes, particularly those requiring minimum ductility and energy dissipation in seismic or impact-resistant structures (e.g., ACI 318, Eurocode 2). The demonstrated efficiency of the CEM method also provides a practical protocol for qualifying waste-derived mixes prior to large-scale applications, which could be translated into material-approval and specification guidelines.

Future research should extend these insights by addressing scale effects by testing full-scale structural members (e.g., bridge decks, slabs, and beams without stirrups) to enhance the generalizability of the results. The long-term durability and service performance of MK–WG concrete must also be examined under realistic exposure conditions, including cyclic loading, freeze–thaw cycles, and chloride ingress, to confirm its viability for real-world use. Complementary numerical modeling efforts are required to calibrate scale-dependent parameters and validate structural performance across multiple dimensions. Critically, translating experimental and numerical outcomes into design-oriented recommendations and sustainable construction guidelines will bridge the gap between laboratory evidence and engineering practice, enabling the systematic adoption of MK–WG concrete in future codes and standards.

**Author Contributions:** Conceptualization, A.J. and J.A.; Methodology, A.J. and H.F.; Software, A.A.; Validation, A.J., A.A. and J.A.; Formal analysis, A.J. and J.A.; Investigation, A.J. and H.F.; Resources, J.A.; Data curation, A.A.; Writing—original draft preparation, A.J.; Writing—review and editing, J.A., C.A.-K. and N.C.; Visualization, A.J.; Supervision, C.A.-K., N.C., A.J. and J.A.; Funding acquisition, J.A. and A.J.; Project administration and submission coordination, C.A.-K., N.C. and A.J. All authors have read and agreed to the published version of the manuscript.

**Funding:** This research was funded by the UNIVERSITY OF BALAMAND (UOB) in Lebanon (grant number RGA/FOE/23-24/001).

**Data Availability Statement:** Data are available from the authors upon request.

**Conflicts of Interest:** The authors declare no conflicts of interest.

## References

1. El-Mir, A.; Nehme, S.; Assaad, J. Feasibility of Concrete Mixtures Containing Coarse and/or Fine Recycled Brick Aggregates. *Mag. Civ. Eng.* **2022**, *116*, 11603. [CrossRef]
2. Nasser Eddine, Z.; Barraj, F.; Khatib, J.; Elkordi, A. From Waste to Resource: Utilizing Municipal Solid Waste Incineration Bottom Ash and Recycled Rubber in Pervious Concrete Pavement. *Innov. Infrastruct. Solut.* **2023**, *8*, 319. [CrossRef]
3. Ghannoum, M.; Shamoun, L.; Nasr, D.; Assaad, J.J.; Riahi, H.; Khatib, J. Efficiency of Stochastic Finite Element Random Fields and Variables to Predict Shear Strength of Fiber-Reinforced Concrete Beams Without Stirrups. *Buildings* **2025**, *15*, 721. [CrossRef]
4. Edlebi, G.A. Review of Enhancing Performance and Sustainability of RC Shear Walls. *Steps Civ. Constr. Environ. Eng.* **2023**, *1*, 38–51. [CrossRef]
5. Awad, Z. Sustainable Restoration Techniques for Historic Buildings in Tyre City. *Steps Civ. Constr. Environ. Eng.* **2023**, *1*, 10–17. [CrossRef]
6. Assaad, J.; Daou, Y.; Harb, J. Use of CEM Approach to Develop and Optimize High-Performance Underwater Concrete. *J. Mater. Civ. Eng. (ASCE)* **2011**, *23*, 1094–1102. [CrossRef]
7. El Mir, A.; Nehme, S.G. Effect of Air Entraining Admixture on the Properties of Self-Compacting Concrete Incorporating Supplementary Cementitious Materials. *Pollack Period.* **2017**, *12*, 85–98. [CrossRef]
8. Barraj, F.; Hatoum, A.; Khatib, J.; Assaad, J.; Castro, A.; Elkordi, A. Uncertainty Analysis for the Dynamic Modulus of Recycled Asphalt Mixtures Using Unclassified Fractionated RAP Materials. *Constr. Build. Mater.* **2024**, *421*, 135721. [CrossRef]
9. Barraj, F.; Hatoum, A.; Assaad, J.J.; Alhakim, G.; Khatib, J.; Assaf, Y.; Elkordi, A. Characterisation of Superpave Recycled Asphalt Mixtures Utilising Optimum Contents of Fatty Amine-Based Asphalt Additive. *Int. J. Mason. Res. Innov.* **2024**, *10*, 76–99. [CrossRef]
10. Nagrockiene, D.; Paliulis, D. The Effect of Crushed Glass and Metakaolin Waste in the Properties of Modified Concrete. *Ceram.—Silik.* **2022**, *66*, 520–526. [CrossRef]
11. Leal, R.B.; Morais, S.; Santos, S. Assessing the Impact of Waste Glass and Metakaolin on the Durability and Mechanical Strength Properties of Concrete. *Matéria* **2024**, *29*, e20240103. [CrossRef]
12. Çelik, A.İ.; Özkılıç, Y.O.; Zeybek, Ö.; Karalar, M.; Qaidi, S.; Ahmad, J.; Burduhos-Nergis, D.D.; Bejinariu, C. Mechanical Behavior of Crushed Waste Glass as Replacement of Aggregates. *Materials* **2022**, *15*, 8093. [CrossRef]
13. Karalar, M.; Başaran, B.; Aksoylu, C.; Zeybek, Ö.; Althaqafi, E.; Beskopylny, A.N.; Stel'makh, S.A.; Shcherban, E.M.; Umiye, O.A.; Özkılıç, Y.O. Utilizing Recycled Glass Powder in Reinforced Concrete Beams: Comparison of Shear Performance. *Sci. Rep.* **2025**, *15*, 6919. [CrossRef]
14. Aksoylu, C.; Başaran, B.; Karalar, M.; Zeybek, Ö.; Althaqafi, E.; Beskopylny, A.N.; Stel'makh, S.A.; Shcherban, E.M.; Umiye, O.A.; Özkılıç, Y.O. Experimental, Theoretical and Digital Image Correlation Methods to Assess Bending Performance of RC Beams with Recycled Glass Powder Replacing Cement. *Sci. Rep.* **2025**, *15*, 25163. [CrossRef]
15. Rachid, T.A.; Dbouk, F.; Hamad, B.; Assaad, J.J. Structural behavior of beams cast using normal and high strength concrete containing blends of ceramic waste powder and blast furnace slag. *Clean. Mater.* **2023**, *7*, 100179. [CrossRef]
16. Nodehi, M.; Mohamad Taghvaee, V. Sustainable Concrete for Circular Economy: A Review on Use of Waste Glass. *Glass Struct. Eng.* **2021**, *7*, 3–22. [CrossRef]
17. Bhat, K.R.; Dumre, G.; Gyawali, T.R. Transforming Waste into Strength: Evaluating Properties of Concrete with Waste Glass Substitution. *Clean. Waste Syst.* **2024**, *9*, 100179. [CrossRef]
18. Bawab, J.; Khatib, J.; Jahami, A.; Elkordi, A.; Ghorbel, E. Structural Performance of Reinforced Concrete Beams Incorporating Cathode-Ray Tube (CRT) Glass Waste. *Buildings* **2021**, *11*, 67. [CrossRef]

19. Zeybek, Ö.; Başaran, B.; Aksoylu, C.; Karalar, M.; Althaqafi, E.; Beskopylny, A.N.; Stel'makh, S.A.; Shcherban, E.M.; Ahmed Umiye, O.; Onuralp Özkılıç, Y. Shear Performance in Reinforced Concrete Beams with Partial Aggregate Substitution Using Waste Glass: A Comparative Analysis via Digital Imaging Processing and a Theoretical Approach. *ACS Omega* **2024**, *9*, 41662–41675. [CrossRef]
20. Amer, A.A.; El-Hoseny, S. Properties and Performance of Metakaolin Pozzolanic Cement Pastes. *J. Therm. Anal. Calorim.* **2017**, *129*, 33–44. [CrossRef]
21. Ravi, N.; Bhavani, P. Strength and Durability Properties of Metakaolin with Partial Replacement of Cement. *IOSR J. Comput. Eng.* **2019**, *21*, 74–83.
22. Lenka, S.; Panda, K.C. Effect of Metakaolin on the Properties of Conventional and Self Compacting Concrete. *Adv. Concr. Constr.* **2017**, *5*, 31–48. [CrossRef]
23. Kaur, A.; Sran, S. Use of Metakaolin as Pozzolanic Material and Partial Replacement with Cement in Concrete (M30). *Asian Rev. Mech. Eng.* **2016**, *5*, 9–13. [CrossRef]
24. Taiye, A.; Olubunmi, A.; Aliyu, S. A Review on the Effect of Pozzolanic Properties of Metakaolin in Concrete. *Int. J. Res. Publ. Rev. J.* **2022**, *3*, 1383–1388.
25. Al-Akhras, N.M. Durability of Metakaolin Concrete to Sulfate Attack. *Cem. Concr. Res.* **2006**, *36*, 1727–1734. [CrossRef]
26. Khatib, J.M.; Baalbaki, O.; ElKordi, A.A. Metakaolin. In *Waste and Supplementary Cementitious Materials in Concrete*; Woodhead Publishing: Cambridge, UK, 2018; pp. 493–511. [CrossRef]
27. Yerramala, A.; Ramachandurdu, C.; Bhaskar Desai, V. Flexural Strength of Metakaolin Ferrocement. *Compos. Part B Eng.* **2013**, *55*, 176–183. [CrossRef]
28. Assaad, J.J.; Saba, M. Use of Metakaolin and Slag Geopolymer Adhesives for Fixing Tiles. *ACI Mater. J.* **2024**, *121*, 3–14. [CrossRef]
29. Homayoonmehr, R.; Ramezanianpour, A.A.; Mirdarsoltany, M. Influence of Metakaolin on Fresh Properties, Mechanical Properties and Corrosion Resistance of Concrete and Its Sustainability Issues: A Review. *J. Build. Eng.* **2021**, *44*, 103011. [CrossRef]
30. *ASTM C150*; Standard Specification for Portland Cement. ASTM International: West Conshohocken, PA, USA, 2024. Available online: https://www.astm.org/c0150_c0150m-24.html (accessed on 2 July 2025).
31. *ASTM C494*; Standard Specification for Chemical Admixtures for Concrete. ASTM International: West Conshohocken, PA, USA, 2017. Available online: https://www.astm.org/c0494_c0494m-17.html (accessed on 2 July 2025).
32. *ASTM C33*; Standard Specification for Concrete Aggregates. ASTM International: West Conshohocken, PA, USA, 2018. Available online: https://www.astm.org/c0033_c0033m-18.html (accessed on 2 July 2025).
33. Assaad, J.; Khayat, K.H. Effect of Coarse Aggregate Characteristics on Lateral Pressure Exerted by Self-Consolidating Concrete. *ACI Mater. J.* **2005**, *102*, 145–153. [CrossRef]
34. *ACI Committee 214*; Guide to Evaluation of Strength Test Results of Concrete (ACI 214R-11) and Commentary. American Concrete Institute: Farmington Hills, MI, USA, 2011.
35. *BS EN 196-8:2005*; Methods of Testing Cement—Part 8: Determination of Strength. British Standards Institution: London, UK, 2005. Available online: https://knowledge.bsigroup.com/products/methods-of-testing-cement-determination-of-strength-2 (accessed on 2 July 2025).
36. *ASTM C642*; Standard Test Method for Density, Absorption, and Voids in Hardened Concrete. ASTM International: West Conshohocken, PA, USA, 2021. Available online: https://www.astm.org/c0642-21.html (accessed on 2 July 2025).
37. *ASTM C39*; Standard Test Method for Compressive Strength of Cylindrical Concrete Specimens. ASTM International: West Conshohocken, PA, USA, 2021. Available online: https://www.astm.org/c0039_c0039m-21.html (accessed on 2 July 2025).
38. *ASTM C469*; Standard Test Method for Static Modulus of Elasticity and Poisson's Ratio of Concrete in Compression. ASTM International: West Conshohocken, PA, USA, 2002. Available online: https://www.astm.org/c0469-02.html (accessed on 2 July 2025).
39. *ASTM C496*; Standard Test Method for Splitting Tensile Strength of Cylindrical Concrete Specimens. ASTM International: West Conshohocken, PA, USA, 1996. Available online: https://www.astm.org/c0496-96.html (accessed on 2 July 2025).
40. *ASTM C1585*; Standard Test Method for Measurement of Rate of Absorption of Water by Hydraulic-Cement Concretes. ASTM International: West Conshohocken, PA, USA, 2020. Available online: https://www.astm.org/c1585-20.html (accessed on 2 July 2025).
41. Anas, S.M.; Alam, M.; Shariq, M. Damage Response of Conventionally Reinforced Two-Way Spanning Concrete Slab under Eccentric Impacting Drop Weight Loading. *Def. Technol.* **2022**, *19*, 12–34. [CrossRef]
42. Jahami, A.; Dayaa, L.; Assaad, J.J.; Baalbaki, O.; Khatib, J. Flexural Strength of Structural Beams Cast Using Combined Normal-Weight and Lightweight Concrete Mixtures. *Buildings* **2024**, *14*, 3787. [CrossRef]
43. Ali, E.E.; Al-Tersawy, S.H. Recycled Glass as a Partial Replacement for Fine Aggregate in Self Compacting Concrete. *Constr. Build. Mater.* **2012**, *35*, 785–791. [CrossRef]
44. Chen, J.J.; Li, Q.H.; Ng, P.L.; Li, L.G.; Kwan, A.K.H. Cement Equivalence of Metakaolin for Workability, Cohesiveness, Strength and Sorptivity of Concrete. *Materials* **2020**, *13*, 1646. [CrossRef]

45. Mydin, M.A.O.; Jagadesh, P.; Bahrami, A.; Majeed, S.S.; Dulaimi, A.; Omar, R. Study on Fresh and Hardened State Properties of Eco-Friendly Foamed Concrete Incorporating Waste Soda-Lime Glass. *Sci. Rep.* **2024**, *14*, 18733. [CrossRef]
46. Sabir, B.B.; Wild, S.; Bai, J. Metakaolin and Calcined Clays as Pozzolans for Concrete: A Review. *Cem. Concr. Compos.* **2001**, *23*, 441–454. [CrossRef]
47. Assaad, J.J.; Saba, M. Use of Seashell and Limestone Fillers in Metakaolin-Based Geopolymers for Masonry Mortars. *Minerals* **2023**, *13*, 186. [CrossRef]
48. Siddique, R.; Klaus, J. Influence of Metakaolin on the Properties of Mortar and Concrete: A Review. *Appl. Clay Sci.* **2009**, *43*, 392–400. [CrossRef]
49. Rakhshanimehr, M.; Esfahani, M.R.; Kianoush, M.R.; Mohammadzadeh, B.A.; Mousavi, S.R. Flexural Ductility of Reinforced Concrete Beams with Lap-Spliced Bars. *Can. J. Civ. Eng.* **2014**, *41*, 594–604. [CrossRef]
50. Redondo-Pérez, N.M.; Redondo-Mosquera, J.D.; Abellán-García, J.A. Comprehensive Overview of Recycled Glass as Mineral Admixture for Circular UHPC Solutions. *Sustainability* **2024**, *16*, 5077. [CrossRef]
51. Assaad, J.; Khayat, K.H. Formwork Pressure of Self-Consolidating Concrete Made with Various Binder Types and Contents. *ACI Mater. J.* **2005**, *102*, 215–223. [CrossRef]
52. Mohamed, A.M.; Tayeh, B.A. Metakaolin in Ultra-High-Performance Concrete: A Critical Review of Its Effectiveness as a Green and Sustainable Admixture. *Case Stud. Constr. Mater.* **2024**, *21*, e03967. [CrossRef]
53. Harrison, E.; Berenjian, A.; Seifan, M. Recycling of Waste Glass as Aggregate in Cement-Based Materials. *Environ. Sci. Ecotechnology* **2020**, *4*, 100064. [CrossRef]
54. Poudel, S.; Bhetuwal, U.; Kharel, P.; Khatiwada, S.; KC, D.; Dhital, S.; Lamichhane, B.; Yadav, S.K.; Suman, S. Waste Glass as Partial Cement Replacement in Sustainable Concrete: Mechanical and Fresh Properties Review. *Buildings* **2025**, *15*, 857. [CrossRef]
55. Usman, M.; Farooq, H.; Umair, M.; Hanif, A. Axial Compressive Behavior of Confined Steel Fiber Reinforced High Strength Concrete. *Constr. Build. Mater.* **2020**, *230*, 117043. [CrossRef]
56. Jayasooriya, D.; Rajeev, P.; Sanjayan, J. Tensile Stress-Strain Models for Steel Fiber Reinforced Concrete. *J. Build. Eng.* **2024**, *96*, 110533. [CrossRef]
57. Babafemi, A.; Šavija, B.; Paul, S.; Anggraini, V. Engineering Properties of Concrete with Waste Recycled Plastic: A Review. *Sustainability* **2018**, *10*, 3875. [CrossRef]
58. Mallum, I.; Mohd.Sam, A.R.; Lim, N.H.A.S.; Omolayo, N. Sustainable Utilization of Waste Glass in Concrete: A Review. *Silicon* **2021**, *14*, 3199–3214. [CrossRef]
59. Autrup, F.; Jørgensen, H.B.; Hoang, L.C. Dowel Action of the Tensile Reinforcement in RC Beams without Shear Reinforcement: Novel Experimental Investigation and Mechanical Modelling. *Eng. Struct.* **2023**, *279*, 115471. [CrossRef]
60. Lakavath, C.; Joshi, S.S.; Prakash, S.S. Investigation of the Effect of Steel Fibers on the Shear Crack-Opening and Crack-Slip Behavior of Prestressed Concrete Beams Using Digital Image Correlation. *Eng. Struct.* **2019**, *193*, 28–42. [CrossRef]
61. Ghali, A.E.A.; El Ezz, N.E.; Hamad, B.; Assaad, J.; Yehya, A. Comparative Study on Shear Strength and Life Cycle Assessment of Reinforced Concrete Beams Containing Different Types of Fibers. *Case Stud. Constr. Mater.* **2023**, *19*, e02497. [CrossRef]
62. Yooprasertchai, E.; Bahrami, A.; Saingam, P.; Hussain, Q.; Ejaz, A.; Joyklad, P. Incorporation of Steel Fibers to Enhance Performance of Sustainable Concrete Made with Waste Brick Aggregates: Experimental and Regression-Based Approaches. *Buildings* **2023**, *13*, 2820. [CrossRef]
63. Gong, C.; Kang, L.; Zhou, W.; Liu, L.; Lei, M. Tensile Performance Test Research of Hybrid Steel Fiber—Reinforced Self-Compacting Concrete. *Materials* **2023**, *16*, 1114. [CrossRef]
64. Avci-Karatas, C.; Celik, O.C.; Eruslu, S.O. Modeling of Buckling Restrained Braces (BRBs) Using Full-Scale Experimental Data. *KSCE J. Civ. Eng.* **2019**, *23*, 4431–4444. [CrossRef]


**Disclaimer/Publisher's Note:** The statements, opinions and data contained in all publications are solely those of the individual author(s) and contributor(s) and not of MDPI and/or the editor(s). MDPI and/or the editor(s) disclaim responsibility for any injury to people or property resulting from any ideas, methods, instructions or products referred to in the content.